

Discovery of widespread non-metastable ammonia masers in the Milky Way

Y. T. Yan (闫耀庭)^{1, *} , C. Henkel^{1,2} , K. M. Menten¹ , T. L. Wilson¹, A. Wootten³ , Y. Gong (龚龑)¹ , F. Wyrowski¹, W. Yang (杨文锦)^{4,1} , A. Brunthaler¹ , A. Kraus¹, and B. Winkel¹

¹ Max-Planck-Institut für Radioastronomie, Auf dem Hügel 69, 53121 Bonn, Germany
e-mail: yyan@mpifr-bonn.mpg.de, astrottingyan@gmail.com

² Xinjiang Astronomical Observatory, Chinese Academy of Sciences, 830011 Urumqi, PR China

³ National Radio Astronomy Observatory, 520 Edgemont Road, Charlottesville, VA 22903-2475, USA

⁴ School of Astronomy & Space Science, Nanjing University, 163 Xianlin Avenue, Nanjing 210023, People's Republic of China

Received XXX; accepted YYY

ABSTRACT

We present the results of a search for ammonia maser emission in 119 Galactic high-mass star-forming regions (HMSFRs) known to host 22 GHz H₂O maser emission. Our survey has led to the discovery of non-metastable NH₃ inversion line masers toward 14 of these sources. This doubles the number of known non-metastable ammonia masers in our Galaxy, including nine new very high excitation (J, K) = (9,6) maser sources. These maser lines, including NH₃ (5,4), (6,4), (6,5), (7,6), (8,6), (9,6), (9,8), (10,8), and (11,9), arise from energy levels of 342 K, 513 K, 465 K, 606 K, 834 K, 1090 K, 942 K, 1226 K, and 1449 K above the ground state. Additionally, we tentatively report a new metastable NH₃ (3,3) maser in G048.49 and an NH₃ (7,7) maser in G029.95. Our observations reveal that all of the newly detected NH₃ maser lines exhibit either blueshifted or redshifted velocities with respect to the source systemic velocities. Among the non-metastable ammonia maser lines, larger velocity distributions, offset from the source systemic velocities, are found in the ortho-NH₃ ($K = 3n$) than in the para-NH₃ ($K \neq 3n$) transitions.

Key words. Masers – ISM: clouds – ISM: H II regions – Radio lines: ISM

1. Introduction

The first maser was obtained from a source of ammonia (NH₃) molecules by Charles H. Townes and his group members in the laboratory (Gordon et al. 1954, 1955). Various maser species were discovered in the interstellar medium (ISM), such as hydroxyl (OH) (Weaver et al. 1965), water (H₂O) (Cheung et al. 1969), and methanol (CH₃OH) (Barrett et al. 1971). Although thermal emission from NH₃ was discovered in 1968 by Cheung et al., the first NH₃ maser in the ISM was detected 14 years later, in the (J, K) = (3,3) metastable ($J = K$) line towards the massive star-forming region W33 (Wilson et al. 1982). The first highly excited non-metastable ($J > K$) ammonia masers were detected by Madden et al. (1986) in the (J, K) = (9,6) and (6,3) lines. So far, a total of 34 NH₃ inversion transitions ($\Delta K = 0$ and $\Delta J = 0$) have been identified as masers in the ISM (see Yan et al. 2022b, and references therein). Even in its rare isotopolog ¹⁵NH₃, maser emission was detected in the (3,3) (Mauersberger et al. 1986), (4,3) and (4,4) transitions (Schilke et al. 1991) but only towards the high-mass star-forming region (HMSFR) NGC 7538. The ammonia transitions identified as masers in the ISM are summarised in Table A.1.

Ammonia masers are rare in the ISM compared to other maser species, i.e., those of OH, H₂O, and CH₃OH. Over the last five decades after the first detection of astronomical masers, numerous successful maser surveys were carried out in different

molecules and led to thousands of detections in the Milky Way. They targeted, for example, OH masers (e.g., te Lintel Hekkert et al. 1989; Lewis 1994; Hu et al. 1994; Sevenster et al. 1997; Caswell 1998; Wolak et al. 2012; Beuther et al. 2019), CH₃OH masers (e.g., Menten 1991; Caswell et al. 1993; Xu et al. 2009; Caswell 2009; Hu et al. 2016; Breen et al. 2016; Yang et al. 2017, 2019; Lu et al. 2019; Nguyen et al. 2022; Yang et al. 2020, 2023), and H₂O masers (e.g., Genzel & Downes 1979; Cesaroni et al. 1988; Menten et al. 1990; Wouterloot et al. 1993; Palagi et al. 1993; Wang et al. 2006; Urquhart et al. 2011; Breen & Ellingsen 2011; Motogi et al. 2011; Walsh et al. 2014; Xi et al. 2015; Titmarsh et al. 2016; Svoboda et al. 2016; Kim et al. 2018; Ladeyschikov et al. 2022a). All of these are collected and can be easily accessed from the online database, Maserdb¹ (Sobolev et al. 2019; Ladeyschikov et al. 2019, 2022b).

So far, ammonia maser lines have only been detected in 32 sources. Among them, metastable NH₃ masers are quite common and have been detected in 22 different regions. Non-metastable ($J > K$) ammonia masers have been found in 14 objects (Yan et al. 2022a,b). Only four sources host both metastable and non-metastable NH₃ masers. These are the HMSFRs DR 21 (Guilloteau et al. 1983; Madden et al. 1986; Mangum & Wootten 1994; Gaume et al. 1996), W51 (Madden et al. 1986; Mauersberger et al. 1987; Zhang & Ho 1995; Henkel et al. 2013), NGC 6334 (Kraemer & Jackson 1995; Beuther et al. 2007; Walsh et al. 2007), and Sgr B2(M) (Mills et al. 2018; Yan et al. 2022a). In Table A.2, we summarise the sources that are known to host am-

* Member of the International Max Planck Research School (IMPRS) for Astronomy and Astrophysics at the universities of Bonn and Cologne.

¹ <https://maserdb.net/>

monia masers. The metastable NH_3 (3,3) masers are thought to be collisionally pumped (e.g., Walmsley & Ungerechts 1983; Flower et al. 1990; Mangum & Wootten 1994; Zhang & Ho 1995; Zhang et al. 1999; McEwen et al. 2016). Pumping scenarios of other NH_3 transitions are still speculative. High angular resolution data show that the excitation of non-metastable NH_3 (9,6) masers in W51, Cepheus A, G34.26+0.15, and the Sgr B2 complex may be related to shocks by outflows or by the expansion of ultracompact (UC) H II regions (Pratap et al. 1991; Yan et al. 2022b,a). Furthermore, the NH_3 (9,6) maser stands out as being the strongest and most variable one in W51-IRS2. Its variability is comparable to the H_2O masers in the region (e.g., Henkel et al. 2013).

There exists no systematic survey to search for ammonia masers so far. Therefore, we selected 119 HMSFRs with high NH_3 column densities ($N_{\text{NH}_3} \geq 10^{15.5} \text{ cm}^{-2}$) that are known to host water masers from previous K-band surveys. The sample is mainly based on the APEX Telescope Large Area Survey of the Galaxy (ATLASGAL, Schuller et al. 2009) catalogs (Wienen et al. 2012, 2018), and the Red MSX Source survey (RMS, Urquhart et al. 2011). Our sample is listed in Table A.3 together with the systemic local standard of rest (LSR) velocities and the source beam averaged NH_3 column densities, which are based on ammonia (1,1), (2,2), and (3,3) thermal emission in previous studies with typical beam sizes of order 32" at Green Bank and 38" at Effelsberg. We performed a K-band line survey with the 100-m Effelsberg telescope of this source sample with the motivations (1): to search for NH_3 maser lines, and (2): to search for the higher metastable ammonia transitions, i.e. the NH_3 (4,4) to (7,7) lines with excitation levels up to 500 K above the ground state to reveal so far poorly studied warm gas components in the HMSFR sources. We also obtained H_2O and CH_3OH maser spectra simultaneously as well as quasi-thermal lines from other molecules. The data allow us to perform a new K-band spectral classification of massive star-forming clumps, uniquely complementing other surveys.

In this letter, we report the discovery of numerous non-metastable NH_3 and two probable metastable NH_3 maser sources in the Milky Way. Results for the high excitation metastable ammonia thermal transitions, the non-metastable ammonia thermal lines, as well as H_2O and CH_3OH maser spectra will be published in future papers.

2. Observations and data reduction

The K-band line survey was performed with the 100-meter Effelsberg telescope² in 2022 November, in 2023 February, April, May, and July. The S14mm double beam secondary focus receiver was employed to simultaneously cover the entire K-band frequency range, i.e. 18.0–26.0 GHz. The receiver band was divided into four 2.5 GHz-wide subbands with the frequency ranges of 18.0–20.5 GHz, 19.9–22.4 GHz, 21.6–24.1 GHz, and 23.5–26.0 GHz. Each subband has 65536 channels, providing a channel width of 38.1 kHz, changing from $\sim 0.62 \text{ km s}^{-1}$ at 18.5 GHz to $\sim 0.44 \text{ km s}^{-1}$ at 26.0 GHz. The observations were performed in position switching mode with the off position 10' in azimuth away from the source. The half power beam width (HPBW) was $49 \times 18.5/\nu(\text{GHz})$ arcseconds, that is 49" at 18.5 GHz, the frequency of the NH_3 (9,6) line. A high spectral resolution backend with 65536 channels and a bandwidth of 300 MHz was employed to measure the new NH_3 (9,6) maser sources, pro-

viding a channel width of 0.07 km s^{-1} at 18.5 GHz. Pointing and focus calibrations were done at the beginning of the observations, during sunset and sunrise, as well as every two hours towards NGC 7027. The calibrator was measured between elevations of 30 and 60 degrees. Pointing was checked using nearby quasars prior to on-source integrations. The elevations of our targets were in a range of 15 to 55 degrees. The system temperatures were 60–130 K on a main-beam brightness temperature, T_{MB} , scale.

We used the GILDAS/CLASS³ package (Pety 2005) to reduce the spectral line data. The data were split into small frequency intervals with bandwidths of 300 MHz and were calibrated based on continuum cross scans of NGC 7027 (Winkel et al. 2012), whose flux density was adopted from Ott et al. (1994). The T_{MB}/S ratios are 1.95 K/Jy, 1.73 K/Jy, and 1.68 K/Jy at 18.5 GHz, 22.2 GHz, and 24.0 GHz, respectively. Calibration uncertainties were estimated to be $\pm 10\%$. All of the NH_3 lines covered in our observations are measured simultaneously, which ensures a good relative calibration.

3. Results and discussion

We detected 15 new ammonia maser sources, resulting in a detection rate of $\sim 13\%$. These maser lines, including NH_3 ($J, K = (5,4), (6,4), (6,5), (7,7), (7,6), (8,6), (9,6), (9,8), (10,8), (11,9)$ and possibly the (3,3) line arise from energy levels of 342 K, 513 K, 465 K, 537 K, 606 K, 834 K, 1090 K, 942 K, 1226 K, 1449 K and 122 K above the ground state. The maser line parameters obtained by Gaussian fits are listed in Table A.4. The masers are identified through three different ways: (1) narrow line widths compared to those of ammonia ($J, K = (1,1)$) thermal emission, (2) blueshifted or redshifted velocities with respect to the source's systemic LSR velocities, and (3) flux density variations. The first method can easily be verified by comparing the widths of putative maser lines with simultaneously observed quasi-thermal transitions.

Figure 1 shows the comparison of line widths of ammonia maser lines to the intrinsic line widths of hyperfine components of the ($J, K = (1,1)$) thermal emission as well as the difference between the systemic velocities of the sources and the maser velocities. We derived the intrinsic line width by using the hyperfine fitting in CLASS for the NH_3 (1,1) line. The line profiles of the NH_3 (1,1) thermal emission and maser transitions are presented in Fig. B.1. All of these maser lines have narrower features than the NH_3 (1,1) thermal emission. This further confirms their maser nature. Furthermore, their velocities are shifted with respect to the source's systemic LSR velocities, by at least 0.7 km s^{-1} , and reaching up to 30 km s^{-1} . This is similar to recent discoveries of non-metastable NH_3 masers with $\delta V \sim 10 \text{ km s}^{-1}$ in Cep A, $\delta V \sim 4 \text{ km s}^{-1}$ in G34.26+0.15, and δV in a range of 0.3 km s^{-1} to 24 km s^{-1} toward the Sgr B2 complex (Yan et al. 2022b,a). Fourteen of the new ammonia maser sources contain non-metastable ammonia masers, which doubles the number of non-metastable ammonia maser detections in our Galaxy. Among the non-metastable ammonia maser lines, larger velocity distributions are found in the ortho- NH_3 ($K = 3n$) than in the para- NH_3 ($K \neq 3n$) transitions. The velocity range of para- NH_3 masers is limited within $\pm 5 \text{ km s}^{-1}$ with respect to the source's systemic velocities, marked as red in Fig. 1. This is enlarged to about $\pm 30 \text{ km s}^{-1}$ for ortho- NH_3 masers.

Among the 14 non-metastable ammonia maser sources, NH_3 (9,6) masers are the most common and are detected in nine ob-

² Based on observations with the 100-meter telescope of the MPIfR (Max-Planck-Institut für Radioastronomie) at Effelsberg.

³ <https://www.iram.fr/IRAMFR/GILDAS/>

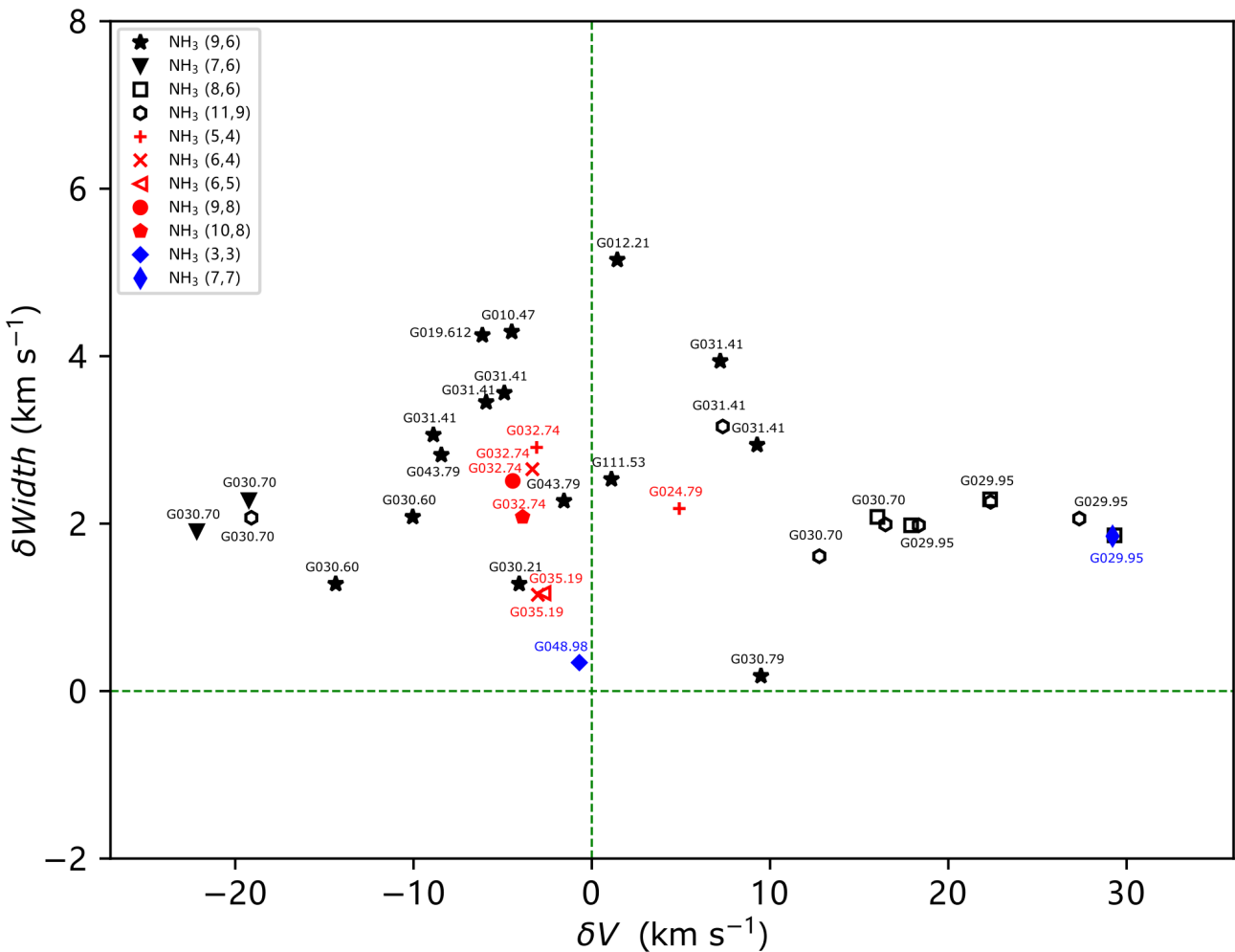


Fig. 1. Comparison of velocities and line widths of ammonia maser lines to the intrinsic line widths of ammonia ($J, K = (1,1)$) thermal emission. The number of data points is substantially larger than the number of newly detected sources due to the occasional presence of more than one maser line in a given source and more than one velocity component in a specific maser line. $\delta V = V_{\text{LSR}}(\text{maser}) - V_{\text{LSR}}(\text{NH}_3(1,1))$, is the deviation from velocities of the NH_3 maser lines to those of $\text{NH}_3(1,1)$ thermal emission. $\delta \text{Width} = \Delta V_{1/2}(\text{NH}_3(1,1)) - \Delta V_{1/2}(\text{maser})$, refers to the difference between the line widths of ammonia maser lines and the intrinsic line widths of an individual NH_3 hyperfine structure component. The green dashed lines indicate positions with zero deviation. The metastable NH_3 transitions are marked in blue. Among the non-metastable NH_3 lines, ortho- NH_3 is presented in black, and para- NH_3 is given in red.

jects. The spectra of $\text{NH}_3(9,6)$ masers are shown in Fig. 2. The observations at different epochs indicate that the flux densities of these $\text{NH}_3(9,6)$ masers vary by at least 50% over time scales of several months. Even within two days, variations were observed in G031.41+0.30 (hereafter G031.41), similar to that detected by Henkel et al. (2013) towards W51-IRS2. The exception is G030.21-0.19 (hereafter G030.21): its $\text{NH}_3(9,6)$ flux density stays constant for 20 days. In order to increase the signal-to-noise ratios (S/N) of $\text{NH}_3(9,6)$ spectra towards G030.21, we average all three measurements at different epochs. The spectra and fitting results are presented in Fig. 2 and in Table A.4, respectively. Five targets, G010.47+0.03 (hereafter G010.47), G012.21-0.10 (hereafter G012.21), G019.61-0.23 (hereafter G019.612), G031.41, and G111.53+0.76 (hereafter G111.53), were also observed in the high spectral resolution mode (Fig. 2). These data show that the $\text{NH}_3(9,6)$ masers contain narrow components with line widths smaller than 1.0 km s^{-1} and some even below the channel width of the wide band spectra (Sect. 2), i.e. smaller than 0.6 km s^{-1} . In eight sources, G010.47, G012.21, G019.612, G030.21, G030.60+0.18 (here-

after G030.60), G030.79+0.20 (hereafter G030.79), G043.79-0.13 (hereafter G043.79), and G111.53, we detect only $\text{NH}_3(9,6)$ masers. Five of these eight targets show only blueshifted (9,6) features, and the other three only have redshifted features. G031.41, the ninth object, is unique in that it hosts both blueshifted and redshifted $\text{NH}_3(9,6)$ maser components.

The $\text{NH}_3(11,9)$ transition with an energy level of 1449 K above the ground state, the highest value in our maser sample, was also detected towards G031.41 (Fig. 3). Its velocity is consistent with a redshifted $\text{NH}_3(9,6)$ maser feature and its flux density decreased from November 2020 to May 2023 by 63%. In addition, $\text{NH}_3(11,9)$ masers were also detected in G029.95-0.02 (hereafter G029.95) and G030.70-0.07 (hereafter G030.70). In G029.95, $\text{NH}_3(8,6)$ and (7,7) masers were also detected (Fig. 4). The flux density of the $\text{NH}_3(7,7)$ maser increased by 55% in three days, while the $\text{NH}_3(8,6)$ and (11,9) maser lines show no obvious variability. Toward G030.70, we also detected $\text{NH}_3(7,6)$ and (8,6) masers. Their spectra are shown in Fig. 5. The $\text{NH}_3(7,6)$ maser stays constant for 20 days. During this time interval, $\text{NH}_3(8,6)$ and (11,9) masers initially showed the same trend, i.e.,

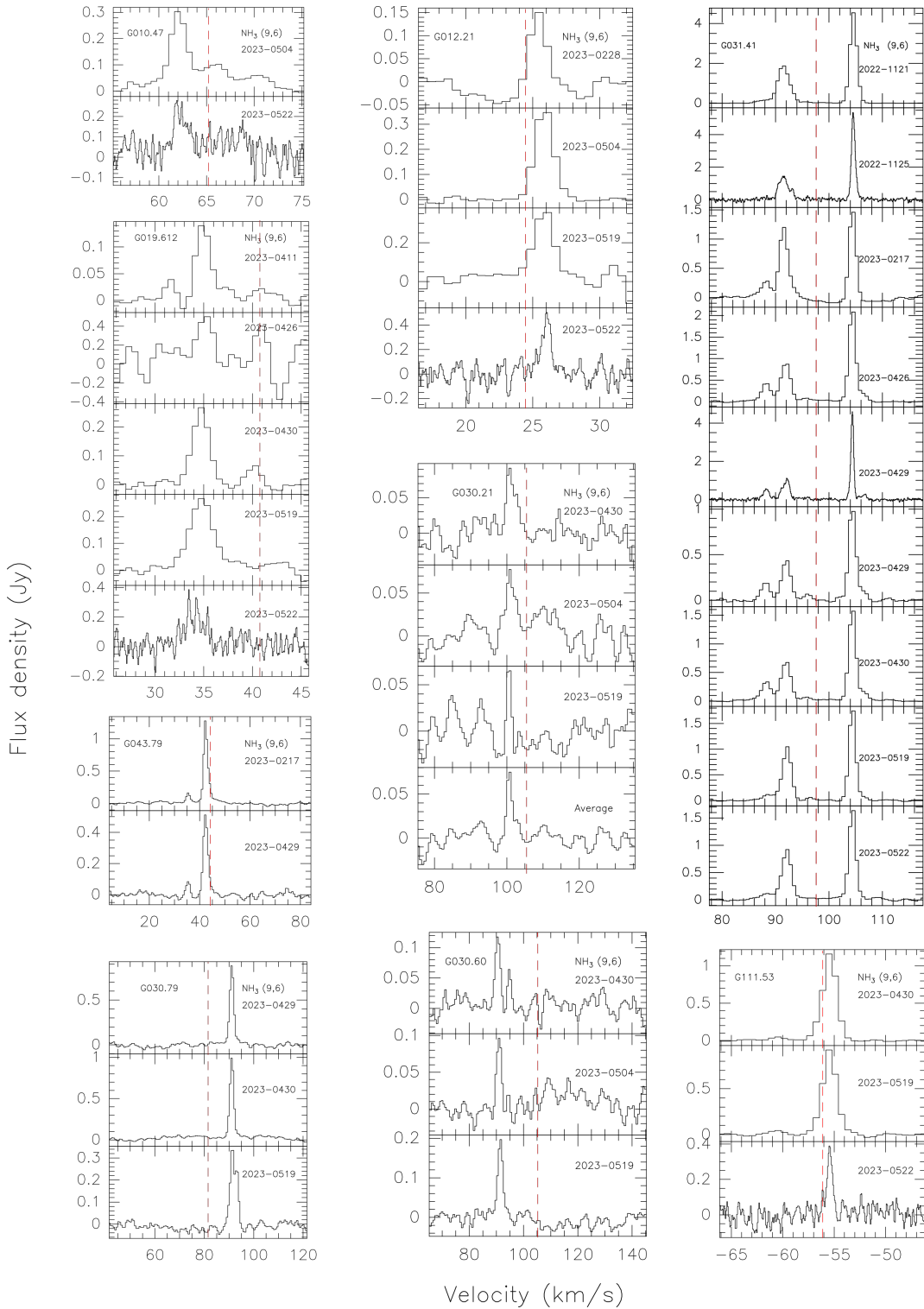


Fig. 2. NH_3 (9,6) spectra observed at different epochs towards nine sources. The dashed red lines indicate the systemic velocities of the sources.

their flux densities are roughly the same from April 30 to May 04 but then decrease between May 04 and 19, 2023. Among the eleven sources mentioned above, G029.95 hosts both ortho- and para- NH_3 masers and the other ten sources only host ortho- NH_3 masers.

Three targets, G024.79+0.08 (hereafter G024.79), G032.74-0.08 (hereafter G032.74), and G035.19-0.74 (hereafter G035.19), only host para- NH_3 masers (Fig. 6). Toward G024.79, we only detected an NH_3 (5,4) maser. Toward

G032.74, four transitions were identified as masers, i.e., the NH_3 (5,4), (6,4), (9,8), and (10,8) lines. Two NH_3 maser lines, (6,4) and (6,5), were detected in G035.19. Variations of flux densities of the NH_3 (5,4) maser in G024.79, of the NH_3 (10,8) maser in G032.74, as well as from the NH_3 (6,5) maser in G035.19 were also observed. These variations amount to 24% or more while the NH_3 (1,1) thermal emissions stay constant at the same time, thus the maser variability appears to be significant.

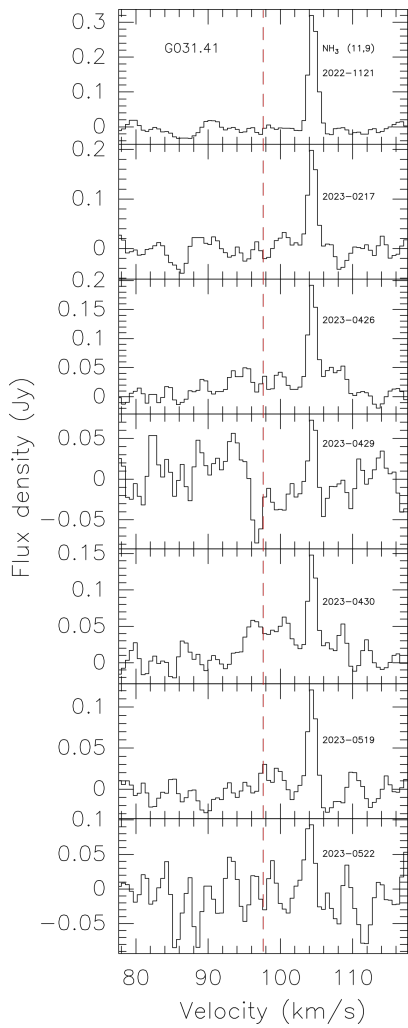


Fig. 3. NH_3 spectra towards G031.41. The dashed red lines indicate the systemic velocity.

The frequencies of the NH_3 (1,1), (2,2) and (3,3) transitions are within a range of only 200 MHz. The peak flux density ratios of NH_3 (3,3)/(1,1) and (3,3)/(2,2) towards G048.98-0.30 (hereafter G048.98) are ~ 0.83 and ~ 1.14 , respectively, based on previous 100-m Green Bank Telescope (GBT) observations in 2010 (Urquhart et al. 2011), while these are ~ 1.57 and ~ 2.22 from our measurements. However, the ratios of NH_3 (1,1)/(2,2) remain consistent, which are ~ 1.38 and ~ 1.42 , within the uncertainties due to noise in these two data sets. This indicates that the NH_3 (3,3) emission in G048.98 has become stronger and likely shows a maser nature. The spectra of NH_3 (1,1), (2,2), and (3,3) towards G048.98 are presented in Fig. 7.

In Fig 8, we compare the velocity ranges of NH_3 and H_2O masers. The velocity range of NH_3 masers is always smaller than that of H_2O masers in each source. There are 12 objects, 80% of our maser sample, for which the velocities of their brightest NH_3 maser feature are similar to that of H_2O masers within $\pm 10 \text{ km s}^{-1}$. For the remaining three targets, G030.79, G029.95, and G030.70, the differences between velocities of their brightest NH_3 maser feature and brightest H_2O maser feature are large, i.e. 11 km s^{-1} , 19 km s^{-1} , and 22 km s^{-1} , respectively.

With the single-dish observations at Effelsberg, the sizes of ammonia masers, the spatial distributions of ammonia masers and thermal emissions cannot be accurately determined. This also excludes realistic determinations of kinetic temperatures,

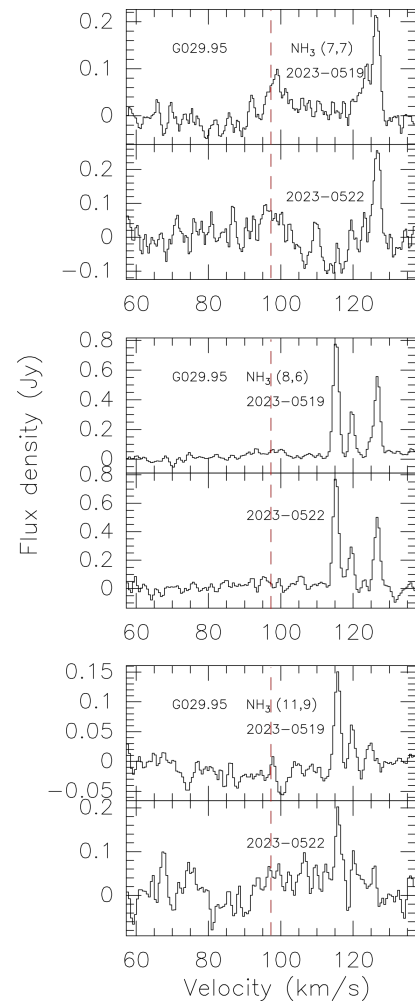


Fig. 4. NH_3 (7,7), (8,6), and (11,9) spectra towards G029.95. The dashed red lines indicate the systemic velocity.

densities, column densities, and estimates of the $\sim 10 \mu\text{m}$ infrared irradiation, potentially causing significant populations of vibrationally excited NH_3 , right at the maser spots. So far, the NH_3 maser pumping processes under debate are collisional excitation, radiative excitation, and radiative excitation combined with infrared line overlap (e.g., Walmsley & Ungerechts 1983; Madden et al. 1986; Brown & Cragg 1991; Wilson & Schilke 1993; Henkel et al. 2013). Velocity offsets with respect to systemic velocities may suggest emission associated with outflows or disks (Yan et al. 2022a). Higher angular resolution observations are mandatory and proposed to provide precise physical positions and sizes of the newly detected ammonia masers. This will lead to a deeper comprehension of the NH_3 maser phenomenon and its connection to sites of massive star formation.

4. Summary

We report the discovery of at least 14 and likely 15 new ammonia maser sources in the Milky Way, based on our K-band line survey with the 100-meter Effelsberg telescope. Our total sample consists of 119 sources exhibiting 22 GHz H_2O maser emission, thus yielding a detection rate in excess of 10%. Fourteen of the newly detected masers are encountered in non-metastable inversion transitions and this doubles the number of non-metastable NH_3 masers in our Galaxy. Metastable ammonia masers are also detected in one or two sources, i.e. an NH_3 (7,7) maser

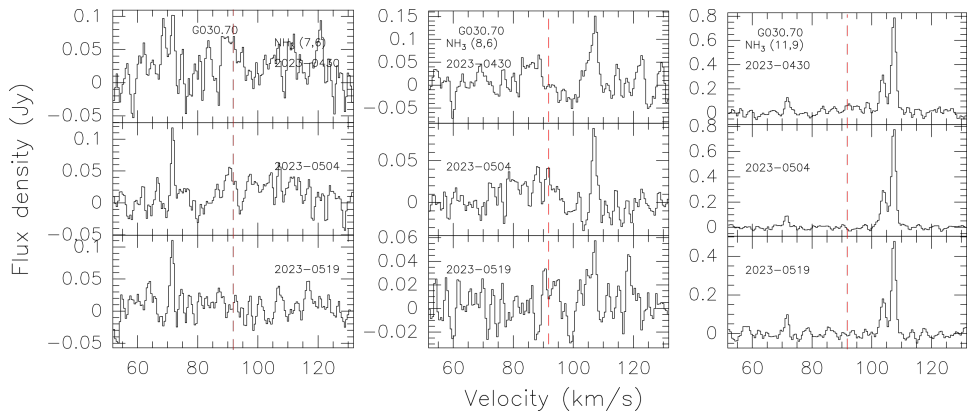


Fig. 5. NH_3 (7,6), (8,6), and (11,9) spectra towards G030.70. The dashed red lines indicate the systemic velocity.

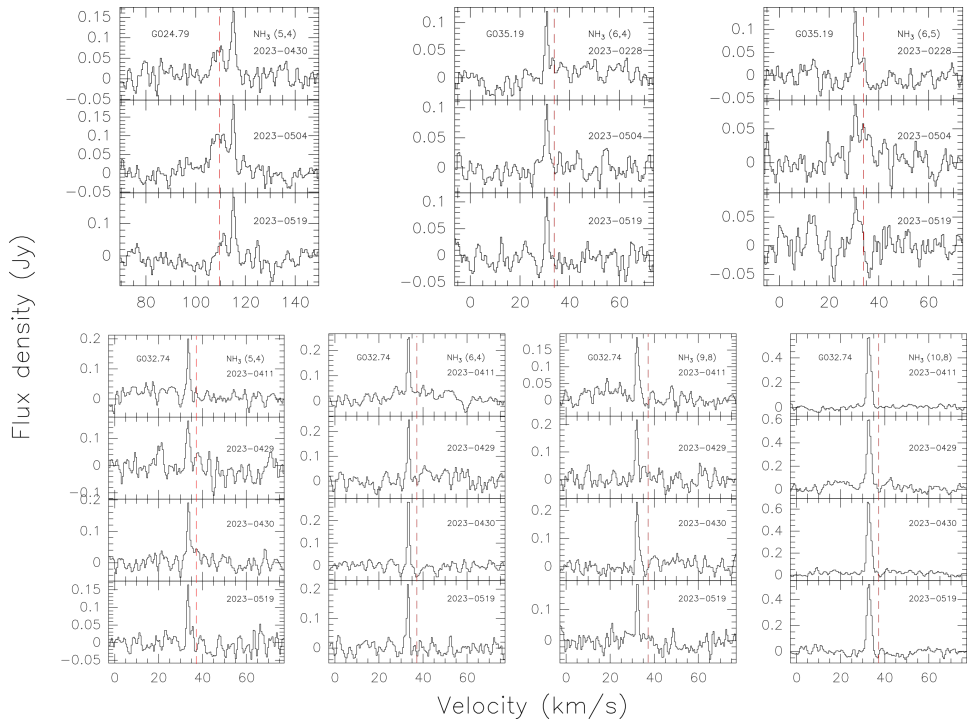


Fig. 6. NH_3 (5,4) spectra towards G024.79, NH_3 (6,4) and (6,5) spectra towards G035.19, as well as NH_3 (5,4), (6,4), (9,8), and (10,8) spectra towards G032.74. The dashed red lines indicate the systemic velocities of the sources.

in G029.95 and likely an NH_3 (3,3) maser in G048.98. Narrow line widths compared to those of ammonia ($J, K = (1, 1)$) thermal emission, as well as variations in flux density, indicate their maser nature. All of the NH_3 masers in our detections have blueshifted or redshifted velocities with respect to the source systemic LSR velocities.

Acknowledgements. The authors want to thank the anonymous referee for providing useful comments, which have improved the quality of the paper. Y.T.Y. is a member of the International Max Planck Research School (IMPRS) for Astronomy and Astrophysics at the Universities of Bonn and Cologne. Y.T.Y. thanks the China Scholarship Council (CSC) for the financial support. Y.T.Y. also thanks his fiancée, Siqi Guo (郭思祺), for her daily and mental supports. We would like to thank the staff at the Effelsberg telescope for their help provided during the observations.

- Breen, S. L. & Ellingsen, S. P. 2011, MNRAS, 416, 178
- Breen, S. L., Ellingsen, S. P., Caswell, J. L., et al. 2016, MNRAS, 459, 4066
- Brogan, C. L., Hunter, T. R., Cyganowski, C. J., et al. 2011, ApJ, 739, L16
- Brown, R. D. & Cragg, D. M. 1991, ApJ, 378, 445
- Caswell, J. L. 1998, MNRAS, 297, 215
- Caswell, J. L. 2009, PASA, 26, 454
- Caswell, J. L., Gardner, F. F., Norris, R. P., et al. 1993, MNRAS, 260, 425
- Cesaroni, R., Palagi, F., Felli, M., et al. 1988, A&AS, 76, 445
- Cesaroni, R., Walmsley, C. M., & Churchwell, E. 1992, A&A, 256, 618
- Cheung, A. C., Rank, D. M., Townes, C. H., Thornton, D. D., & Welch, W. J. 1968, Phys. Rev. Lett., 21, 1701
- Cheung, A. C., Rank, D. M., Townes, C. H., Thornton, D. D., & Welch, W. J. 1969, Nature, 221, 626
- Endres, C. P., Schlemmer, S., Schilke, P., Stutzki, J., & Müller, H. S. P. 2016, Journal of Molecular Spectroscopy, 327, 95
- Flower, D. R., Offer, A., & Schilke, P. 1990, MNRAS, 244, 4P
- Galván-Madrid, R., Keto, E., Zhang, Q., et al. 2009, ApJ, 706, 1036
- Gaume, R. A., Wilson, T. L., & Johnston, K. J. 1996, ApJ, 457, L47
- Genzel, R. & Downes, D. 1979, A&A, 72, 234
- Gordon, J. P., Zeiger, H. J., & Townes, C. H. 1954, Phys. Rev., 95, 282
- Gordon, J. P., Zeiger, H. J., & Townes, C. H. 1955, Phys. Rev., 99, 1264
- Guilloteau, S., Wilson, T. L., Martin, R. N., Batria, W., & Pauls, T. A. 1983, A&A, 124, 322
- Henkel, C., Wilson, T. L., Asiri, H., & Mauersberger, R. 2013, A&A, 549, A90

References

- Barrett, A. H., Schwartz, P. R., & Waters, J. W. 1971, ApJ, 168, L101
- Beuther, H., Walsh, A., Wang, Y., et al. 2019, A&A, 628, A90
- Beuther, H., Walsh, A. J., Thorwirth, S., et al. 2007, A&A, 466, 989

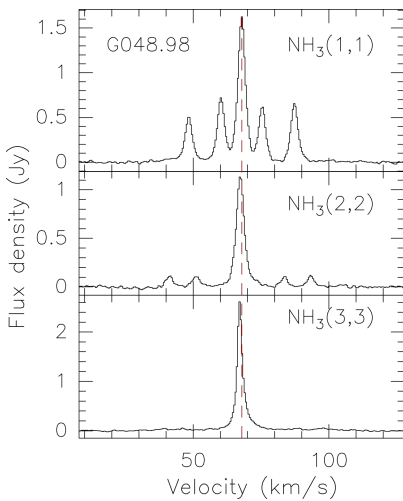


Fig. 7. NH_3 (1,1), (2,2), and (3,3) spectra towards G048.98. The dashed red lines indicate the systemic velocity.

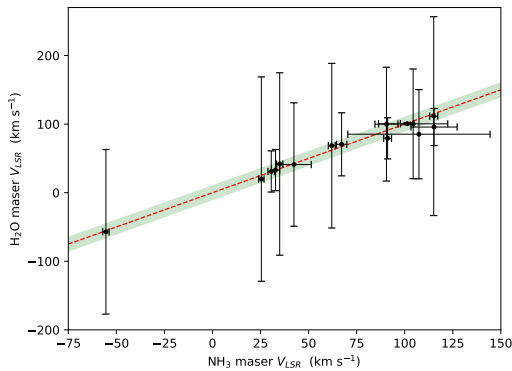


Fig. 8. Comparison of the velocity ranges of NH_3 and H_2O masers. Dots indicate the velocities of bright NH_3 and H_2O maser features. Error bars show the velocity ranges in detected NH_3 and H_2O masers. The dashed line marks locations where the velocity of NH_3 equals that of a water maser. The green region shows the $\pm 10 \text{ km s}^{-1}$ zone.

- Hoffman, I. M. 2012, ApJ, 759, 76
 Hoffman, I. M. & Joyce, S. A. 2014, ApJ, 782, 83
 Hogge, T. G., Jackson, J. M., Allingham, D., et al. 2019, ApJ, 887, 79
 Hu, B., Menten, K. M., Wu, Y., et al. 2016, ApJ, 833, 18
 Hu, J. Y., te Lintel Hekkert, P., Slijkhuis, F., et al. 1994, A&AS, 103, 301
 Hunter, T. R., Brogan, C. L., Indebetouw, R., & Cyganowski, C. J. 2008, ApJ, 680, 1271
 Kim, C.-H., Kim, K.-T., & Park, Y.-S. 2018, ApJS, 236, 31
 Kraemer, K. E. & Jackson, J. M. 1995, ApJ, 439, L9
 Ladeyschikov, D. A., Bayandina, O. S., & Sobolev, A. M. 2019, AJ, 158, 233
 Ladeyschikov, D. A., Gong, Y., Sobolev, A. M., et al. 2022a, ApJS, 261, 14
 Ladeyschikov, D. A., Sobolev, A. M., Bayandina, O. S., & Shakhvorostova, N. N. 2022b, AJ, 163, 124
 Lewis, B. M. 1994, ApJS, 93, 549
 Lu, X., Mills, E. A. C., Ginsburg, A., et al. 2019, ApJS, 244, 35
 Madden, S. C., Irvine, W. M., Matthews, H. E., Brown, R. D., & Godfrey, P. D. 1986, ApJ, 300, L79
 Mangum, J. G. & Wootten, A. 1994, ApJ, 428, L33
 Mauersberger, R., Henkel, C., & Wilson, T. L. 1987, A&A, 173, 352
 Mauersberger, R., Wilson, T. L., & Henkel, C. 1986, A&A, 160, L13
 Mauersberger, R., Wilson, T. L., & Henkel, C. 1988, A&A, 201, 123
 McCarthy, T. P., Breen, S. L., Kaczmarek, J. F., et al. 2023, MNRAS, 522, 4728
 McEwen, B. C., Pihlström, Y. M., & SJouwerman, L. O. 2016, ApJ, 826, 189
 Mei, Y., Chen, X., Shen, Z.-Q., & Li, B. 2020, ApJ, 898, 157
 Menten, K. M. 1991, ApJ, 380, L75
 Menten, K. M., Melnick, G. J., & Phillips, T. G. 1990, ApJ, 350, L41
 Mills, E. A. C., Ginsburg, A., Clements, A. R., et al. 2018, ApJ, 869, L14
 Motogi, K., Sorai, K., Honma, M., et al. 2011, MNRAS, 417, 238

- Müller, H. S. P., Schlöder, F., Stutzki, J., & Winnewisser, G. 2005, Journal of Molecular Structure, 742, 215
 Nguyen, H., Rugel, M. R., Murugesan, C., et al. 2022, A&A, 666, A59
 Ott, M., Witzel, A., Quirrenbach, A., et al. 1994, A&A, 284, 331
 Palagi, F., Cesaroni, R., Comoretto, G., Felli, M., & Natale, V. 1993, A&AS, 101, 153
 Pety, J. 2005, in SF2A-2005: Semaine de l’Astrophysique Francaise, ed. F. Casoli, T. Contini, J. M. Hameury, & L. Pagani, 721
 Pickett, H. M., Poynter, R. L., Cohen, E. A., et al. 1998, J. Quant. Spectr. Rad. Transf., 60, 883
 Pratap, P., Menten, K. M., Reid, M. J., Moran, J. M., & Walmsley, C. M. 1991, ApJ, 373, L13
 Schilke, P., Walmsley, C. M., & Mauersberger, R. 1991, A&A, 247, 516
 Schuller, F., Menten, K. M., Contreras, Y., et al. 2009, A&A, 504, 415
 Sevenster, M. N., Chapman, J. M., Habing, H. J., Killeen, N. E. B., & Lindqvist, M. 1997, A&AS, 122, 79
 Sobolev, A. M., Ladeyschikov, D. A., & Nakashima, J.-i. 2019, Research in Astronomy and Astrophysics, 19, 034
 Svoboda, B. E., Shirley, Y. L., Battersby, C., et al. 2016, ApJ, 822, 59
 te Lintel Hekkert, P., Versteeghe-Hensel, H. A., Habing, H. J., & Wiertz, M. 1989, A&AS, 78, 399
 Timmarsh, A. M., Ellingsen, S. P., Breen, S. L., Caswell, J. L., & Voronkov, M. A. 2016, MNRAS, 459, 157
 Towner, A. P. M., Brogan, C. L., Hunter, T. R., & Cyganowski, C. J. 2021, ApJ, 923, 263
 Urquhart, J. S., Morgan, L. K., Figura, C. C., et al. 2011, MNRAS, 418, 1689
 Walmsley, C. M. & Ungerechts, H. 1983, A&A, 122, 164
 Walsh, A. J., Breen, S. L., Britton, T., et al. 2011, MNRAS, 416, 1764
 Walsh, A. J., Longmore, S. N., Thorwirth, S., Urquhart, J. S., & Purcell, C. R. 2007, MNRAS, 382, L35
 Walsh, A. J., Purcell, C. R., Longmore, S. N., et al. 2014, MNRAS, 442, 2240
 Wang, K., Zhang, Q., Wu, Y., Li, H.-b., & Zhang, H. 2012, ApJ, 745, L30
 Wang, Y., Zhang, Q., Rathborne, J. M., Jackson, J., & Wu, Y. 2006, ApJ, 651, L125
 Weaver, H., Williams, D. R. W., Dieter, N. H., & Lum, W. T. 1965, Nature, 208, 29
 Wienen, M., Wyrowski, F., Menten, K. M., et al. 2018, A&A, 609, A125
 Wienen, M., Wyrowski, F., Schuller, F., et al. 2012, A&A, 544, A146
 Wilson, T. L., Batrla, W., & Pauls, T. A. 1982, A&A, 110, L20
 Wilson, T. L. & Schilke, P. 1993, Ammonia masers in the interstellar medium., ed. A. W. Clegg & G. E. Nedoluha, Vol. 412, 123–126
 Winkel, B., Kraus, A., & Bach, U. 2012, A&A, 540, A140
 Wolak, P., Szymczak, M., & Gérard, E. 2012, A&A, 537, A5
 Wouterloot, J. G. A., Brand, J., & Fiegle, K. 1993, A&AS, 98, 589
 Xi, H., Zhou, J., Esimbek, J., et al. 2015, MNRAS, 453, 4203
 Xu, Y., Voronkov, M. A., Pandian, J. D., et al. 2009, A&A, 507, 1117
 Yan, Y. T., Henkel, C., Menten, K. M., et al. 2022a, A&A, 666, L15
 Yan, Y. T., Henkel, C., Menten, K. M., et al. 2022b, A&A, 659, A5
 Yang, K., Chen, X., Shen, Z.-Q., et al. 2019, ApJS, 241, 18
 Yang, K., Chen, X., Shen, Z.-Q., et al. 2017, ApJ, 846, 160
 Yang, W., Gong, Y., Menten, K. M., et al. 2023, A&A, 675, A112
 Yang, W., Xu, Y., Choi, Y. K., et al. 2020, ApJS, 248, 18
 Zhang, Q. & Ho, P. T. P. 1995, ApJ, 450, L63
 Zhang, Q., Hunter, T. R., Sridharan, T. K., & Cesaroni, R. 1999, ApJ, 527, L117

Appendix A: Tables

Table A.1. Catalog of ammonia transitions having been identified as masers in the ISM.

Number	Transition (J, K)	ν (MHz)	E_{low}/k (K)	E_{up}/k (K)	Discovery source & Reference
1	(1,1)	23694.49550	22.12769	23.26484	DR21, a
2	(2,2)	23722.63330	63.30956	64.44806	Sgr B2(M), b
3	(3,3)	23870.12920	122.39346	123.53904	W33, c
4	(5,5)	24532.98870	294.19337	295.37076	G9.26+0.19, d
5	(5,4)	22653.02200	342.22451	343.31167	W51-IRS2, e
6	(5,3)	21285.27500	379.43682	380.45835	W51-IRS2, f
7	(6,6)	25056.02500	406.85658	408.05908	NGC6334, g
8	(6,5)	22732.42900	465.55043	466.64141	W3(OH), h
9	(6,4)	20994.61700	513.33957	514.34714	Sgr B2(N), i
10	(6,3)	19757.53800	550.36513	551.31333	NGC7538, j
11	(6,2)	18884.69500	576.73689	577.64321	W51-IRS2, f
12	(6,1)	18391.56200	592.52954	593.41219	Sgr B2(N), i
13	(7,7)	25715.18200	537.31664	538.55077	W51-IRS2, f
14	(7,6)	22924.94000	606.67824	607.77846	W51-IRS2, f
15	(7,5)	20804.83000	665.02736	666.02583	W51-IRS2, e
16	(7,4)	19218.46500	712.53838	713.46072	W51-IRS2, f
17	(7,3)	18017.33700	749.35187	750.21656	Sgr B2(N), i
18	(8,6)	20719.22100	834.46640	835.46076	NGC6334, k
19	(8,5)	18808.50700	892.42835	893.33101	W51-IRS2, f
20	(8,4)	17378.11000	939.62715	940.46116	Sgr B2(N), i
21	(8,3)	16455.09900	976.19662	976.98634	Sgr B2(N), i
22	(9,9)	27477.94300	851.45423	852.77295	W51-IRS2, f
23	(9,8)	23657.47100	942.18255	943.31792	W51-IRS2, e
24	(9,7)	20735.45200	1021.61682	1022.61196	W51-IRS2, f
25	(9,6)	18499.39000	1089.99977	1090.88760	W51, NGC7538, W49, DR21(OH), j
26	(9,5)	16798.13400	1147.53483	1148.34101	Sgr B2(N), i
27	(9,4)	15523.90000	1194.38934	1195.13437	Sgr B2(N), i
28	(9,3)	14376.81700	1230.70171	1231.39168	Sgr B2(N), i
29	(10,9)	24205.28700	1136.46581	1137.62748	W51-IRS2, f
30	(10,8)	20852.52700	1226.43274	1227.43349	W51-IRS2, e
31	(10,7)	18285.43400	1305.21064	1306.08820	W51-IRS2, f
32	(10,6)	16319.32400	1373.03592	1373.81912	NGC7538, l
33	(11,9)	21070.73900	1448.86263	1449.87386	NGC6334, k
34	(12,12)	31424.94300	1454.90272	1456.41088	W51-IRS2, f
35	$^{15}\text{NH}_3$ (3,3)	22789.42170	124.64182	125.73554	NGC7538, m
36	$^{15}\text{NH}_3$ (4,3)	21637.89450	238.70035	239.73880	NGC7538, n
37	$^{15}\text{NH}_3$ (4,4)	23046.01580	202.51921	203.62523	NGC7538, n

Notes. The parameters of ammonia lines are taken from the Jet Propulsion Laboratory (JPL) molecular line catalog (Pickett et al. 1998, <https://spec.jpl.nasa.gov/>) and the Cologne Database for Molecular Spectroscopy (CDMS, Müller et al. 2005; Endres et al. 2016). For the last column, see a Gaume et al. (1996), b Mills et al. (2018), c Wilson et al. (1982), d Cesaroni et al. (1992), e Mauersberger et al. (1987), f Henkel et al. (2013), g Beuther et al. (2007), h Mauersberger et al. (1988), i Mei et al. (2020), j Madden et al. (1986), k Walsh et al. (2007), l Hoffman (2012), m Mauersberger et al. (1986), n Schilke et al. (1991).

Table A.2. A catalog of sources hosting ammonia masers.

Number	source	metastable	non-metastable	source type	Discovery Reference
		(J = K)	(J > K)		
1	W33	Y	N	SFR	a
2	DR 21	Y	Y	SFR	b, c, d, e
3	NGC7538	N	Y	SFR	c, f, g
4	W51	Y	Y	SFR	c, h, i, j

continued.

Number	source	metastable	non-metastable	source type	Discovery Reference
		(J = K)	(J > K)		
5	W49	N	Y	SFR	c
6	W3(OH)	N	Y	SFR	k
7	G9.26+0.19	Y	N	SFR	l
8	NGC6334	Y	Y	SFR	m, n, o
9	IRAS20126+4104	Y	N	SFR	p
10	G05.89-0.39	Y	N	SFR	q
11	G19.61-0.23	N	Y	SFR	r
12	G23.33-0.30	Y	N	SNR	r, s
13	G030.7206-00.0826	Y	N	SFR	t
14	G20.08-0.14N	Y	N	SFR	u
15	G35.03+0.35	Y	N	SFR	v
16	G28.34+0.06	Y	N	SFR	w
17	W44	Y	N	SNR	x
18	G5.7-0.0	Y	N	SNR	x
19	W51C	Y	N	SNR	x
20	IC443	Y	N	SNR	x
21	Sgr B2(M)	Y	Y	SFR	y, z
22	Sgr B2(N)	N	Y	SFR	z, z1
23	G10.34-0.14	Y	N	SFR	z2
24	G14.33-0.64	Y	N	SFR	z2
25	G18.89-0.47	Y	N	SFR	z2
26	G19.36-0.03	Y	N	SFR	z2
27	G28.83-0.25	Y	N	SFR	z2
28	CepA	N	Y	SFR	z3
29	G34.26+0.15	N	Y	SFR	z3
30	Sgr B2(NS)	N	Y	SFR	z
31	Sgr B2(S)	N	Y	SFR	z
32	G358.931-0.030	N	Y	SFR	z4
33	G010.47+0.03	N	Y	SFR	this work
34	G012.21-0.10	N	Y	SFR	this work
35	G019.61-0.23	N	Y	SFR	this work
36	G024.79+0.08	N	Y	SFR	this work
37	G029.95-0.02	Y	Y	SFR	this work
38	G030.21-0.19	N	Y	SFR	this work
39	G030.60+0.18	N	Y	SFR	this work
40	G030.70-0.07	N	Y	SFR	this work
41	G030.79+0.20	N	Y	SFR	this work
42	G031.41+0.30	N	Y	SFR	this work
43	G032.74-0.08	N	Y	SFR	this work
44	G035.19-0.74	N	Y	SFR	this work
45	G043.79-0.13	N	Y	SFR	this work
46	G048.98-0.30	Y	N	SFR	this work
47	G111.53+0.76	N	Y	SFR	this work
count		24	28		

Notes. SFR: star-forming region, SNR: supernova remnant. Y indicates a detection and N marks a non-detection. a [Wilson et al. \(1982\)](#), b [Guilloteau et al. \(1983\)](#), c [Madden et al. \(1986\)](#), d [Mangum & Wootten \(1994\)](#), e [Gaume et al. \(1996\)](#), f [Hoffman \(2012\)](#), g [Hoffman & Joyce \(2014\)](#), h [Zhang & Ho \(1995\)](#), i [Mauersberger et al. \(1987\)](#), j [Henkel et al. \(2013\)](#), k [Mauersberger et al. \(1988\)](#), l [Cesaroni et al. \(1992\)](#), m [Kraemer & Jackson \(1995\)](#), n [Beuther et al. \(2007\)](#), o [Walsh et al. \(2007\)](#), p [Zhang et al. \(1999\)](#), q [Hunter et al. \(2008\)](#), r [Walsh et al. \(2011\)](#), s [Hogge et al. \(2019\)](#), t [Urquhart et al. \(2011\)](#), u [Galván-Madrid et al. \(2009\)](#), v [Brogan et al. \(2011\)](#), w [Wang et al. \(2012\)](#), x [McEwen et al. \(2016\)](#), y [Mills et al. \(2018\)](#), z [Yan et al. \(2022a\)](#), z1 [Mei et al. \(2020\)](#), z2 [Towner et al. \(2021\)](#), z3 [Yan et al. \(2022b\)](#), z4 [McCarthy et al. \(2023\)](#)

Table A.3. Our sample of 119 observed sources.

Source	R.A.	Dec.	V_{LSR}	$\log(N_{\text{NH}_3})$
	(h m s)	(° ' '')	(km s ⁻¹)	(cm ⁻²)
G010.47+0.03	18 08 38.1	-19 51 50	65.20	16.01
G010.63-0.34	18 10 18.6	-19 54 17	-4.57	15.56

Table A.3. continued.

Source	R.A. (<i>h m s</i>)	Dec. ($^{\circ} \ '$ $''$)	V_{LSR} (km s $^{-1}$)	Log(N_{NH_3}) (cm $^{-2}$)
G010.68-0.03	18 09 15.8	-19 42 27	51.04	15.55
G010.99-0.08	18 10 06.5	-19 27 46	29.67	15.67
G011.90-0.14	18 12 10.8	-18 41 36	38.41	15.79
G011.94-0.61	18 14 00.9	-18 53 24	36.72	15.63
G012.20-0.03	18 12 23.6	-18 22 52	50.86	15.70
G012.21-0.10	18 12 39.2	-18 24 22	24.46	15.61
G012.68-0.18	18 13 54.2	-18 01 46	55.37	15.84
G012.89+0.49	18 11 51.1	-17 31 27	34.30	15.62
G012.91-0.26	18 14 39.1	-17 51 58	38.05	15.55
G013.18+0.06	18 14 00.9	-17 28 41	49.06	15.67
G013.66-0.60	18 17 24.3	-17 22 12	46.75	15.67
G013.87+0.28	18 14 35.5	-16 45 41	48.52	15.53
G014.10+0.09	18 15 46.2	-16 39 09	9.15	15.54
G014.20-0.19	18 16 58.8	-16 42 05	39.91	15.53
G014.49-0.14	18 17 22.0	-16 25 00	39.57	15.81
G014.60+0.02	18 16 59.7	-16 14 51	26.62	15.60
G014.61+0.01	18 17 02.1	-16 14 36	25.14	15.62
G014.99-0.67	18 20 19.4	-16 13 31	19.43	16.00
G016.87-2.15	18 29 24.3	-15 15 42	18.58	16.00
G018.17-0.30	18 25 07.5	-13 14 33	49.14	15.55
G018.46-0.00	18 24 35.8	-12 51 08	53.72	15.69
G018.66+0.04	18 24 50.4	-12 39 21	81.05	15.70
G018.89-0.47	18 27 07.6	-12 41 40	66.28	15.66
G019.07-0.29	18 26 48.1	-12 26 28	65.48	15.70
G019.47+0.17	18 25 54.5	-11 52 35	21.03	15.88
G019.61-0.14	18 27 17.4	-11 53 56	58.65	15.81
G019.61-0.23	18 27 38.1	-11 56 39	40.76	15.80
G019.61-0.26	18 27 43.8	-11 57 06	42.91	15.52
G019.88-0.53	18 29 14.3	-11 50 30	43.48	15.60
G019.92-0.26	18 28 19.2	-11 40 36	64.70	15.72
G020.36-0.01	18 28 15.8	-11 10 26	52.15	15.53
G020.74-0.09	18 29 16.9	-10 52 27	58.21	15.60
G020.98+0.10	18 29 02.7	-10 34 28	18.34	15.52
G022.35+0.06	18 31 44.2	-09 22 17	84.18	15.60
G023.01-0.41	18 34 39.7	-09 00 42	77.97	15.66
G023.20+0.00	18 33 32.8	-08 39 10	76.17	15.55
G023.21-0.38	18 34 54.9	-08 49 17	77.87	15.68
G023.26+0.07	18 33 24.7	-08 33 50	77.93	15.60
G023.48+0.10	18 33 43.0	-08 21 30	85.41	15.67
G024.18+0.12	18 34 57.2	-07 43 27	113.53	15.80
G024.41+0.10	18 35 26.2	-07 31 44	113.62	15.54
G024.44-0.23	18 36 40.7	-07 39 27	58.11	15.63
G024.49-0.04	18 36 05.6	-07 31 31	109.74	15.58
G024.67-0.15	18 36 50.0	-07 24 49	112.97	15.62
G024.79+0.08	18 36 12.4	-07 12 10	109.49	15.69
G024.80+0.10	18 36 10.7	-07 11 18	109.93	15.70
G024.92+0.08	18 36 27.1	-07 05 10	43.76	15.54
G025.46-0.21	18 38 30.1	-06 44 29	118.95	15.60
G025.72+0.05	18 38 02.8	-06 23 46	99.19	15.70
G027.37-0.17	18 41 51.2	-05 01 43	91.05	15.51
G027.56+0.08	18 41 19.8	-04 44 21	84.21	15.65
G028.20-0.05	18 42 58.1	-04 13 58	96.08	15.53
G028.61+0.02	18 43 28.9	-03 50 17	102.02	15.70
G028.65+0.03	18 43 31.1	-03 47 54	103.59	15.57
G028.81+0.17	18 43 18.8	-03 35 26	105.80	15.56
G028.82+0.36	18 42 37.2	-03 29 42	86.40	15.51
G028.84+0.49	18 42 12.3	-03 24 54	86.43	15.53
G029.40-0.09	18 45 18.9	-03 11 19	105.58	15.53
G029.59-0.61	18 47 31.7	-03 15 14	76.51	15.70
G029.81+2.22	18 37 50.5	-01 45 39	45.42	15.60

Table A.3. continued.

Source	R.A. (<i>h m s</i>)	Dec. ($^{\circ} \ '$ $''$)	V_{LSR} (km s $^{-1}$)	Log(N_{NH_3}) (cm $^{-2}$)
G029.91-0.05	18 46 05.5	-02 42 27	99.71	15.56
G029.93-0.06	18 46 10.7	-02 41 52	99.20	15.54
G029.95-0.02	18 46 04.2	-02 39 21	97.24	15.60
G030.01-0.27	18 47 03.8	-02 43 39	103.38	15.71
G030.21-0.19	18 47 08.3	-02 30 34	105.43	15.57
G030.30+0.05	18 46 26.0	-02 19 11	108.07	15.60
G030.42-0.23	18 47 40.3	-02 20 29	105.61	15.57
G030.59-0.04	18 47 18.9	-02 06 16	41.60	15.70
G030.60+0.18	18 46 33.3	-01 59 35	105.21	15.86
G030.68-0.07	18 47 35.6	-02 02 08	91.58	15.64
G030.70-0.07	18 47 36.1	-02 00 59	91.76	15.91
G030.73-0.07	18 47 40.3	-01 59 30	91.71	15.67
G030.74-0.06	18 47 38.9	-01 58 32	96.12	15.55
G030.77-0.22	18 48 16.1	-02 01 11	104.90	15.54
G030.79+0.20	18 46 47.6	-01 49 02	81.51	15.59
G030.83-0.06	18 47 48.9	-01 54 01	97.02	15.61
G031.28+0.06	18 48 12.1	-01 26 31	109.04	15.60
G031.41+0.30	18 47 34.6	-01 13 01	97.60	15.89
G032.04+0.06	18 49 36.6	-00 45 44	95.29	15.80
G032.15+0.13	18 49 31.8	-00 38 07	93.95	15.70
G032.45+0.39	18 49 11.6	-00 14 57	49.17	15.65
G032.74-0.08	18 51 21.8	-00 12 08	37.17	15.72
G032.82-0.33	18 52 24.6	-00 14 58	79.30	15.70
G033.21-0.01	18 51 58.2	+00 14 31	99.96	15.58
G033.91+0.11	18 52 50.5	+00 55 29	107.46	15.60
G034.40+0.23	18 53 18.6	+01 24 49	57.42	15.80
G034.82+0.35	18 53 37.9	+01 50 31	56.90	15.60
G035.19-0.74	18 58 13.1	+01 40 39	33.71	15.60
G035.23-0.36	18 56 54.1	+01 52 45	52.90	15.59
G035.47+0.14	18 55 34.4	+02 19 09	76.91	15.60
G035.58-0.03	18 56 22.6	+02 20 30	52.37	15.60
G035.75+0.15	18 56 02.1	+02 34 39	83.52	15.64
G036.41+0.02	18 57 41.9	+03 06 06	57.77	15.80
G037.55+0.20	18 59 09.9	+04 12 15	85.06	15.70
G037.74-0.11	19 00 36.9	+04 13 23	46.45	15.54
G037.76-0.22	19 01 02.2	+04 12 06	64.39	15.59
G037.82+0.41	18 58 53.9	+04 32 18	17.97	15.58
G037.87-0.60	19 02 36.1	+04 06 59	50.71	15.60
G038.69-0.45	19 03 35.5	+04 55 11	50.86	15.54
G040.43+0.70	19 02 39.6	+06 59 11	12.71	15.64
G040.60-0.72	19 08 03.3	+06 29 12	65.70	15.70
G043.18-0.52	19 12 08.8	+08 52 05	58.03	15.60
G043.31-0.21	19 11 16.9	+09 07 30	59.55	15.70
G043.79-0.13	19 11 54.1	+09 35 50	44.11	15.60
G043.89-0.78	19 14 26.1	+09 22 35	54.01	15.60
G045.46+0.04	19 14 25.6	+11 09 27	62.13	15.70
G045.80-0.36	19 16 31.1	+11 16 12	58.42	15.67
G045.94-0.40	19 16 56.0	+11 21 54	61.74	15.65
G048.98-0.30	19 22 26.2	+14 06 38	67.66	15.60
G049.27-0.34	19 23 07.0	+14 20 15	68.44	15.54
G049.45-0.35	19 23 33.1	+14 29 43	67.49	16.00
G051.68+0.72	19 23 58.6	+16 57 44	4.80	15.63
G053.18+0.21	19 28 51.9	+18 02 37	1.59	15.61
G069.54-0.97	20 10 08.9	+31 31 34	11.18	15.70
G078.98+0.35	20 31 10.7	+40 03 14	5.98	15.60
G108.76-0.99	22 58 47.5	+58 45 01	-51.46	15.60
G111.53+0.76	23 13 43.9	+61 26 58	-56.13	15.70

Notes. Column (1): source name; Columns (2) and (3): Equatorial coordinates (*J2000*); Column (4): Local Standard of Rest velocity; Column (5): NH₃ column densities.

Table A.4. New ammonia masers.

Source	transition	ν (J, K)	Epoch	Channel spacing (km s $^{-1}$)	S_ν (Jy)	rms (Jy)	$\int S_\nu dv$ (Jy km s $^{-1}$)	V_{LSR}	$\Delta V_{1/2}$	
									(km s $^{-1}$)	(1,1)*
G010.47	(9,6)	18499.390	2023, May 04	0.62	0.25	0.015	0.47 ± 0.03	62.05 ± 0.05	1.79 ± 0.11	6.08 ± 0.48
			2023, May 22	0.07	0.17	0.061	0.08 ± 0.03	61.81 ± 0.04	0.43 ± 0.10	
				0.12			0.02 ± 0.01	62.39 ± 0.04	0.15 ± 0.07	
				0.13			0.28 ± 0.06	62.58 ± 0.19	2.00 ± 0.39	
G012.21	(9,6)	18499.390	2023, Feb. 28	0.62	0.17	0.013	0.25 ± 0.02	25.42 ± 0.07	1.40 ± 0.16	6.55 ± 0.48
			2023, May 04	0.62	0.37	0.008	0.66 ± 0.01	25.86 ± 0.02	1.67 ± 0.04	
			2023, May 19	0.62	0.37	0.061	0.98 ± 0.15	25.83 ± 0.15	2.50 ± 0.55	
			2023, May 22	0.07	0.44	0.077	0.39 ± 0.03	26.02 ± 0.03	0.82 ± 0.08	
G019.612	(9,6)	18499.390	2023, Apr. 11	0.62	0.14	0.011	0.25 ± 0.02	34.96 ± 0.06	1.68 ± 0.15	5.93 ± 0.48
			2023, Apr. 26	0.62	...	0.185	
			2023, Apr. 30	0.62	0.27	0.019	0.59 ± 0.04	34.71 ± 0.07	2.07 ± 0.16	
			2023, May 19	0.62	0.27	0.037	1.60 ± 0.10	34.81 ± 0.15	3.68 ± 0.50	
			2023, May 22	0.07	0.18	0.055	0.05 ± 0.01	32.41 ± 0.03	0.27 ± 0.06	
					0.31		0.17 ± 0.03	33.50 ± 0.03	0.53 ± 0.15	
					0.28		0.16 ± 0.04	34.33 ± 0.04	0.52 ± 0.18	
					0.16		0.12 ± 0.03	35.28 ± 0.10	0.69 ± 0.21	
G024.79	(5,4)	22653.022	2023, Apr. 30	0.50	0.14	0.019	0.32 ± 0.03	115.10 ± 0.10	2.10 ± 0.25	3.37 ± 0.48
			2023, May 04	0.50	0.15	0.018	0.19 ± 0.04	115.21 ± 0.07	1.19 ± 0.19	
			2023, May 19	0.50	0.18	0.022	0.33 ± 0.03	115.28 ± 0.08	1.70 ± 0.21	
G029.95	(7,7)	25715.182	2023, May 19	0.44	0.18	0.017	0.36 ± 0.05	126.56 ± 0.07	1.87 ± 0.18	3.72 ± 0.48
			2023, May 22	0.44	0.28	0.030	0.71 ± 0.07	126.59 ± 0.11	2.36 ± 0.28	
			2023, May 19	0.55	0.78	0.017	1.45 ± 0.03	115.26 ± 0.02	1.74 ± 0.03	
					0.30		0.45 ± 0.02	119.69 ± 0.04	1.43 ± 0.09	
G030.21	(9,6)	18499.390	2023, May 22	0.54	0.18	0.035	0.48 ± 0.08	115.87 ± 0.18	2.51 ± 0.57	
			2023, Apr. 30	0.62	0.08	0.015	0.32 ± 0.03	101.25 ± 0.18	3.51 ± 0.46	3.13 ± 0.05
			2023, May 04	0.62	0.07	0.014	0.25 ± 0.04	101.15 ± 0.26	3.54 ± 0.60	
			2023, May 19	0.62	0.07	0.016	0.09 ± 0.02	100.72 ± 0.15	1.18 ± 0.28	
			average	0.62	0.07	0.007	0.14 ± 0.01	100.77 ± 0.09	1.85 ± 0.24	
G030.60	(9,6)	18499.390	2023, Apr. 30	0.62	0.11	0.008	0.25 ± 0.02	90.50 ± 0.08	2.07 ± 0.18	3.35 ± 0.48
				0.06			0.08 ± 0.02	94.82 ± 0.13	1.27 ± 0.26	
				0.62	0.09	0.008	0.19 ± 0.02	90.97 ± 0.10	1.89 ± 0.19	
				0.62	0.20	0.010	0.53 ± 0.03	91.46 ± 0.06	2.50 ± 0.17	
G030.70	(7,6)	22924.940	2023, Apr. 30	0.50	0.09	0.023	0.18 ± 0.04	68.77 ± 0.21	1.86 ± 0.59	3.77 ± 0.01
				0.10			0.16 ± 0.04	71.69 ± 0.18	1.49 ± 0.38	
				0.50	0.12	0.018	0.14 ± 0.02	71.72 ± 0.08	1.12 ± 0.17	
				0.50	0.12	0.019	0.17 ± 0.02	71.47 ± 0.10	1.35 ± 0.21	
			2023, Apr. 30	0.55	0.12	0.022	0.38 ± 0.05	106.91 ± 0.20	2.87 ± 0.49	
			2023, May 04	0.50	0.10	0.012	0.17 ± 0.03	106.95 ± 0.13	1.69 ± 0.30	
			2023, May 19	0.50	0.05	0.015	0.06 ± 0.02	107.02 ± 0.25	1.32 ± 0.55	
			2023, May 19	0.54	0.12	0.026	0.23 ± 0.05	71.83 ± 0.18	1.70 ± 0.41	
G030.79	(9,6)	18499.390	2023, Apr. 29	0.62	0.89	0.019	1.94 ± 0.04	91.10 ± 0.02	2.04 ± 0.05	2.22 ± 0.48
			2023, Apr. 30	0.62	0.98	0.017	2.03 ± 0.04	91.10 ± 0.02	1.95 ± 0.04	
			2023, May 19	0.62	0.33	0.012	1.16 ± 0.03	91.83 ± 0.05	3.32 ± 0.10	
				0.54	0.11	0.022	0.15 ± 0.02	71.56 ± 0.11	1.30 ± 0.24	
				0.18			0.40 ± 0.03	103.84 ± 0.07	2.02 ± 0.18	
				0.50			0.86 ± 0.03	107.37 ± 0.03	1.61 ± 0.06	
G031.41	(9,6)	18499.390	2022, Nov. 21	0.62	1.86	0.006	5.32 ± 0.05	91.51 ± 0.01	2.69 ± 0.03	4.57 ± 0.48
				4.51			7.56 ± 0.04	104.60 ± 0.01	1.57 ± 0.01	
			2022, Nov. 25	0.07	0.62	0.006	0.41 ± 0.07	90.53 ± 0.07	0.61 ± 0.07	
				1.47			2.15 ± 0.07	91.56 ± 0.07	1.37 ± 0.07	
				0.56			0.53 ± 0.07	93.07 ± 0.07	0.88 ± 0.07	
				5.21			4.68 ± 0.07	104.58 ± 0.07	0.84 ± 0.07	
			2023, Feb. 17	0.62	0.28	0.019	0.64 ± 0.08	88.09 ± 0.14	2.12 ± 0.35	

Table A.4. continued.

Source	transition	ν	Epoch	Channel spacing (km s $^{-1}$)	S_ν	rms	$\int S_\nu dv$	V_{LSR}	$\Delta V_{1/2}$ (1,1)*
	(J, K)	(MHz)		(Jy)	(Jy)		(Jy km s $^{-1}$)		(km s $^{-1}$)
(11,9)	21070.739	2022, Nov. 21	2023, Apr. 26	0.62	1.20	2.52 ± 0.06	91.56 ± 0.03	1.98 ± 0.08	
				0.62	1.54	2.37 ± 0.06	104.43 ± 0.02	1.45 ± 0.04	
				0.62	0.44	0.008	1.01 ± 0.07	88.24 ± 0.06	2.15 ± 0.19
				0.62	0.92	2.09 ± 0.06	91.92 ± 0.03	2.13 ± 0.08	
			2023, Apr. 29	0.62	2.18	3.54 ± 0.05	104.39 ± 0.01	1.52 ± 0.02	
				0.62	0.21	0.44 ± 0.04	88.14 ± 0.09	2.03 ± 0.23	
				0.62	0.45	0.95 ± 0.04	92.02 ± 0.03	2.00 ± 0.10	
				0.62	1.03	1.75 ± 0.03	104.40 ± 0.01	1.60 ± 0.04	
			2023, Apr. 29	0.07	0.48	0.043	0.59 ± 0.05	88.29 ± 0.07	1.16 ± 0.07
				0.07	0.39	0.34 ± 0.05	91.13 ± 0.07	0.80 ± 0.07	
				0.07	0.97	1.23 ± 0.05	92.17 ± 0.07	1.19 ± 0.07	
				0.07	4.53	3.05 ± 0.02	104.39 ± 0.07	0.63 ± 0.07	
G032.74	(5,4)	22653.022	2023, Apr. 30	0.62	0.24	0.35 ± 0.03	106.43 ± 0.07	1.38 ± 0.07	
				0.62	0.33	0.010	0.84 ± 0.06	88.25 ± 0.08	2.37 ± 0.24
				0.62	0.69	1.59 ± 0.06	91.98 ± 0.04	2.14 ± 0.10	
				0.62	1.62	2.78 ± 0.05	104.41 ± 0.01	1.62 ± 0.03	
			2023, May 19	0.62	0.11	0.009	0.30 ± 0.20	88.91 ± 0.62	2.59 ± 0.62
				0.62	1.03	2.07 ± 0.20	91.14 ± 0.62	1.88 ± 0.62	
				0.62	1.80	2.88 ± 0.20	104.40 ± 0.62	1.50 ± 0.62	
				0.62	0.11	0.019	0.38 ± 0.19	88.10 ± 0.62	3.22 ± 0.62
			2023, May 22	0.62	0.86	2.14 ± 0.19	92.11 ± 0.62	2.32 ± 0.62	
				0.62	1.71	2.88 ± 0.19	104.40 ± 0.62	1.58 ± 0.62	
				0.54	0.35	0.012	0.52 ± 0.02	104.52 ± 0.02	1.41 ± 0.06
				0.54	0.21	0.019	0.31 ± 0.02	104.44 ± 0.05	1.41 ± 0.13
G035.19	(6,4)	20994.617	2023, Apr. 26	0.54	0.18	0.012	0.36 ± 0.05	104.49 ± 0.10	1.84 ± 0.34
				0.54	0.54	...	0.021
				0.54	0.14	0.015	0.23 ± 0.02	104.46 ± 0.07	1.51 ± 0.20
				0.54	0.12	0.012	0.15 ± 0.02	104.37 ± 0.07	1.20 ± 0.14
			2023, May 19	0.54	0.13	0.038	0.39 ± 0.11	103.91 ± 0.32	2.94 ± 1.27
				0.54	0.17	0.020	0.25 ± 0.03	33.45 ± 0.07	1.39 ± 0.19
				0.50	0.26	0.014	0.43 ± 0.03	33.37 ± 0.06	1.56 ± 0.16
				0.50	0.27	0.021	0.38 ± 0.04	33.39 ± 0.07	1.34 ± 0.18
			2023, Apr. 30	0.50	0.33	0.012	0.41 ± 0.02	33.36 ± 0.03	1.17 ± 0.07
				0.50	0.22	0.019	0.30 ± 0.02	33.19 ± 0.05	1.28 ± 0.12
				0.48	0.18	0.020	0.32 ± 0.03	32.27 ± 0.07	1.70 ± 0.15
				0.48	0.22	0.023	0.33 ± 0.03	32.01 ± 0.06	1.41 ± 0.14
G043.79	(9,8)	23657.471	2023, Apr. 30	0.48	0.23	0.016	0.39 ± 0.03	32.26 ± 0.06	1.58 ± 0.13
				0.48	0.20	0.019	0.32 ± 0.03	32.33 ± 0.06	1.46 ± 0.15
				0.55	0.58	0.015	1.32 ± 0.02	32.82 ± 0.02	2.13 ± 0.04
				0.55	0.60	0.033	1.41 ± 0.06	32.79 ± 0.04	2.22 ± 0.11
			2023, May 19	0.55	0.66	0.019	1.47 ± 0.03	32.77 ± 0.02	2.11 ± 0.05
				0.55	0.53	0.023	1.21 ± 0.04	32.82 ± 0.04	2.16 ± 0.08
				0.54	0.12	0.013	0.22 ± 0.03	30.75 ± 0.10	1.73 ± 0.31
				0.54	0.10	0.011	0.22 ± 0.03	30.78 ± 0.11	2.07 ± 0.35
G111.53	(9,6)	22732.429	2023, May 19	0.54	0.12	0.017	0.17 ± 0.02	30.85 ± 0.08	1.39 ± 0.19
				0.50	0.13	0.017	0.24 ± 0.03	30.57 ± 0.08	1.71 ± 0.25
				0.50	0.07	0.013	0.17 ± 0.07	30.32 ± 0.21	2.41 ± 0.53
			2023, Feb. 28	0.50	0.06	0.019	0.21 ± 0.04	31.01 ± 0.30	3.04 ± 0.59
				0.62	1.21	0.014	0.39 ± 0.05	35.49 ± 0.14	2.39 ± 0.43
				0.62	0.09	0.013	2.64 ± 0.04	42.37 ± 0.02	2.04 ± 0.04
G048.98	(3,3)	18499.390	2023, Feb. 17	0.62	0.51	0.013	0.16 ± 0.02	35.36 ± 0.11	1.65 ± 0.23
				0.62	1.16	0.011	2.03 ± 0.02	-55.43 ± 0.01	1.65 ± 0.02
				0.62	0.91	0.012	1.62 ± 0.02	-55.45 ± 0.01	1.67 ± 0.03
				0.07	0.36	0.040	0.24 ± 0.01	-55.43 ± 0.02	0.63 ± 0.05
(2,2)	(2,2)	23870.100	2022, Nov. 21	0.48	2.40	0.015	6.93 ± 0.08	67.17 ± 0.01	2.71 ± 0.04
				0.48	1.08	0.015	4.33 ± 0.04	67.35 ± 0.01	3.75 ± 0.04
				0.48	1.53	0.009	5.89 ± 0.14	67.87 ± 0.48	3.61 ± 0.48
									3.05 ± 0.4

Notes. * The intrinsic line widths of ammonia (J, K) = (1,1) thermal emission.

Appendix B: Figures

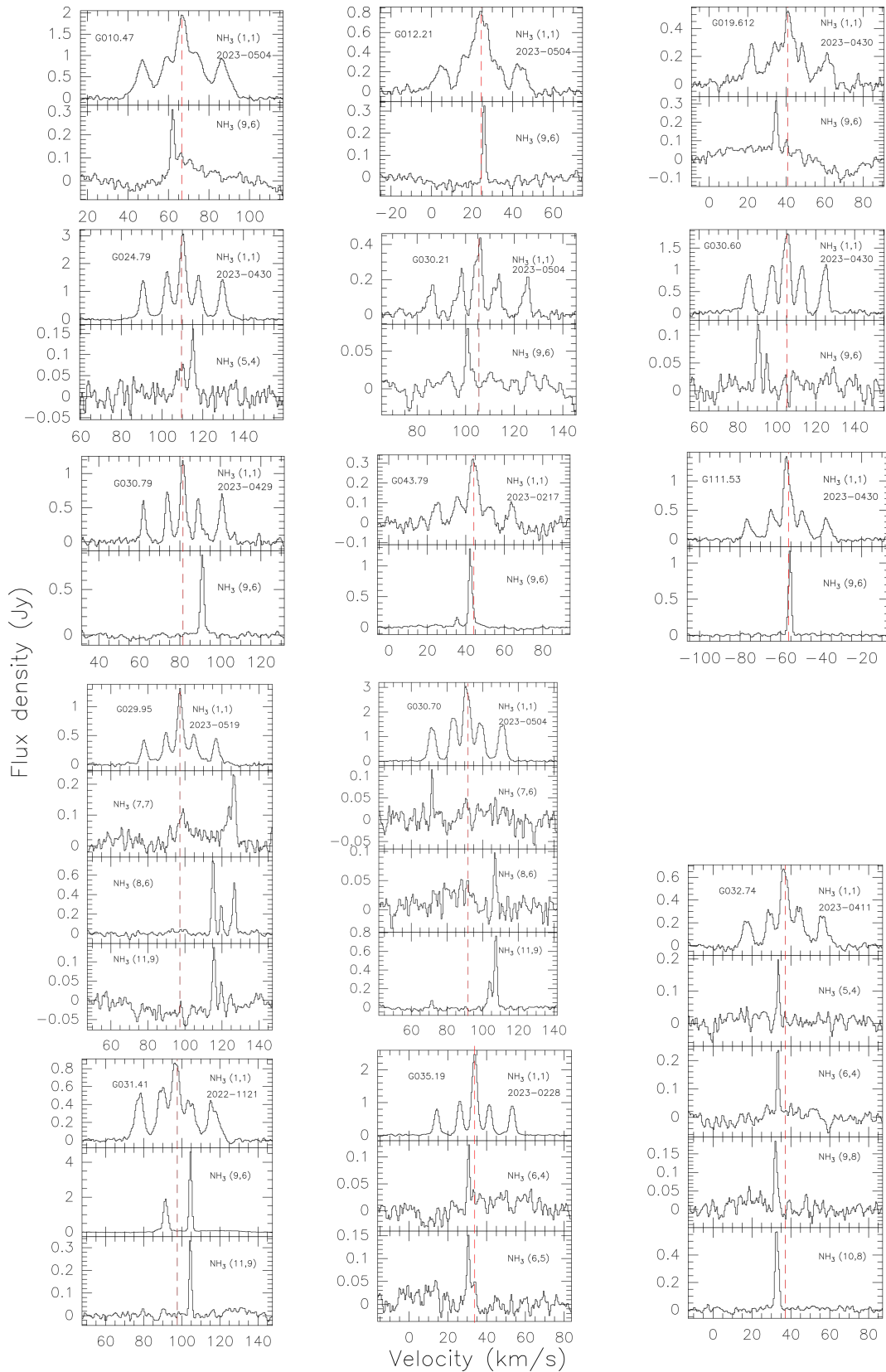


Fig. B.1. Line profiles of NH_3 (1,1) thermal emission and maser transitions in 14 sources. The dashed red lines indicate the systemic velocities of the sources.